Università degli Studi di Padova
Dipartimento di Fisica ed Astronomia
Corso di Laurea in
Fisica

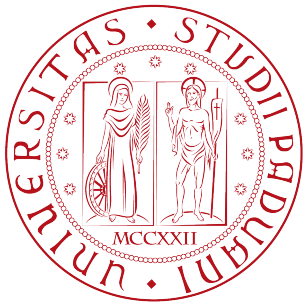

Tesi di Laurea Triennale

Characterisation of the first prototype of the neutron detector array NEDA

Relatori:
prof. S. Lunardi
dott. J.J. Valiente Dobón

Laureando:
Alberto Da Re
Matr. 1007556

Anno Accademico 2013/2014

Contents

1 Introduction

In the present work the set up and characterization of the first detector prototype of NEDA (NEutron Detector Array) will be discussed. NEDA is a neutron detector of new generation that is being built by an European collaboration, for nuclear structure studies far from stability. In fact, for nuclides with neutrons to protons ratio very far from the valley of stability (see Fig. 1.1), several new phenomena not fully described by the present models start to appear. These *exotic nuclei* have structural properties (e.g. nuclear radii, binding energies, magic numbers) which do not follow the ones of nuclei along stability. In the last years the interest of the scientific community in the study of exotic nuclei is increased, not only because it may lead to the discovery of new elements, but also it may provide useful results to reinforce the current nuclear models. There are also considerable astrophysical interests in both proton- and neutron-rich nuclei because of their roles in the *rp*- and *r*-processes, respectively.

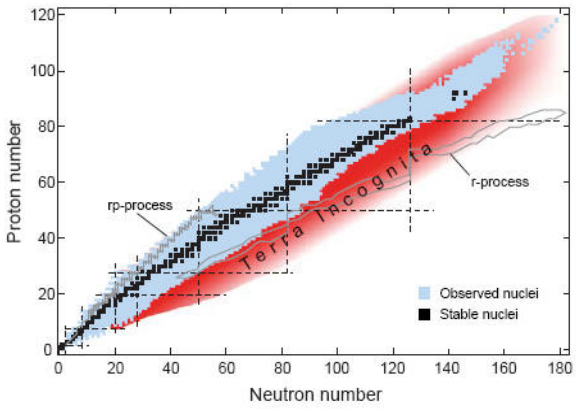

Figure 1.1: Segrè chart, or chart of nuclides.

An exotic nucleus can be produced in a nuclear reaction where an incoming ion, accelerated to an energy of a few MeV per nucleon, hits a target of another isotope. If the energy overcomes the Coulomb barrier, the fusion of the two nuclei occurs and a compound nucleus is produced, which carries a large excess of energy and angular momentum. In the de-excitation process particles such as neutrons, protons, or α are emitted and subsequently γ-ray emission occurs, until the ground state of the final nucleus is reached (see Fig. 1.2). This process is called "*fusion-evaporation reaction*". Exotic nuclei can be also produced in many other kinds of nuclear reactions, such as multi-nucleon transfer, fragmentation, fission, etc. More recently radioactive ion beams (RIB) have been developed to produce even more exotic nuclei. Many of such RIB facilities are under construction around the world. In Europe, we mention the SPES facility at Legnaro, the SPIRAL2 facility at GANIL and the HIE-ISOLDE one at CERN.

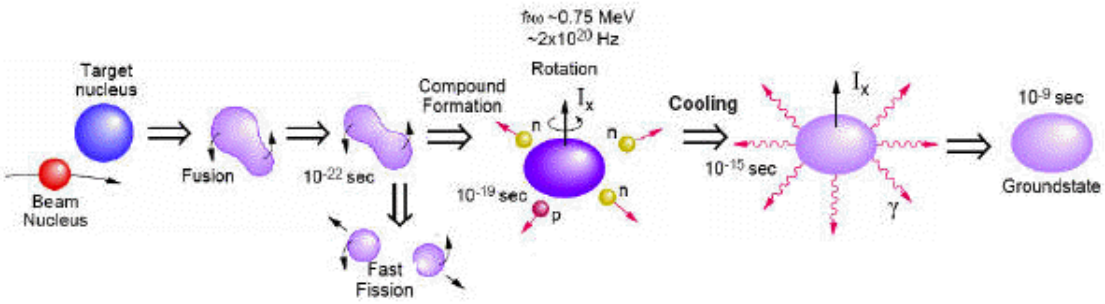

Figure 1.2: Fusion-evaporation reaction scheme.

Especially when unknown regions of the chart of nuclides are explored, a unique identification of the residual nuclides, produced in the reaction after the decay of the compound nucleus, is essential. Detecting all, or at least as many as possible, of the emitted light particles allow to determine the Z and A of the residual nuclides.

Besides the light charged particle detection (p, α, etc.) neutron detection is fundamental especially if one wants to study proton-rich nuclei. The current 1π neutron detector array Neutron Wall [1] that was built for this purpose consists of 50 closely packed liquid scintillation detectors, with two different shapes (hexagonal and pentagonal). Since 2005 it is located at GANIL where it is used together with the high-purity germanium (HPGe) detector EXOGAM [2], and the charged particle detector array DIAMANT. The Neutron Wall detectors are filled with the liquid scintillator BC-501A to a total volume of 150 liters. The hexagonal detectors are subdivided into three individual segments, and the pentagonal ones into five segments. However, with such a closely packed array a problem arises: the neutrons can scatter from one detector to another and produce a signal in more than one detector at the same time. This *cross-talk* effect complicates the clear and efficient determination of the number of emitted neutrons. To overcome this problem, when two neighbor detectors give a signal in coincidence, it is rejected, a method known as *neighbor rejection*. For the Neutron Wall the loss due to neighbor rejection is about 44%.

Another important aspect to be considered is the neutron-γ discrimination, whose efficiency has to be optimized for experiments with RIBs. Indeed, during such experiments, the γ ray background will be much higher than the one occurring with stable beams, as a consequence of the radioactive character of the beam ions and their consequent decay. It has been shown that even a small amount of γ rays misinterpreted as neutrons dramatically reduces the quality of the cross-talk rejection.

Table 1.1 shows a comparison between the characteristics and performances of the Neutron Wall and those designed and predicted for NEDA. The NEDA array is designed to be used with the new generation GALILEO/AGATA/EXOGAM2 [3] [4] [2] and PARIS γ detector arrays in reactions induced by both intense stable beams as well as radioactive

ion beams, for nuclear structure studies both on the neutron-rich side and proton-rich side of the stability line. NEDA will replace the Neutron Wall array. The design goal is to build an array with the highest possible neutron detection efficiency, excellent neutron-γ discrimination, and a very small neutron-scattering probability.

A study of the best configuration of the whole detector array was also performed [5], considering the neutron efficiencies of the different neutron channels as a bench mark, and taking into account the constraints and the total volume of the scintillator. Indeed, the size of the entire NEDA detector array is limited by the space constraints in the experimental hall, but also by the maximum flight time of neutrons to the detectors. So it was concluded that the largest practical inner diameter of the NEDA array is about 1 m [5] [6]. NEDA will have a Staircase 2π geometry, which is created by a modification of the flat geometry: each cell of the flat geometry is moved along the beam line axis to create a "spherical" shape, covering a solid angle of 2π (see Fig. 1.3).

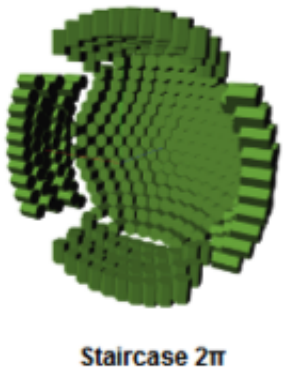

Figure 1.3: Final NEDA geometry. It is formed by around 350 equal hexagonal detectors.

Table 1.1: Specifications of NEDA compared to those of Neutron Wall. Efficiencies are estimated for symmetric fusion-evaporation reactions.

Parameter	**NEDA**	**Neutron Wall**
Type of detector	Liquid scintillator	Liquid scintillator
Type of liquid	EJ301	BC501A
Number detectors	~ 350	50
Solid angle coverage	$\sim 2\pi$	1π
Target-detector distance	~ 100 cm	50 cm
Detector thickness	20 cm	15 cm
Scintillation light detector	5" PM	5" PM
Electronics	Fast sampling ADC	Analogue NIM units
PSA algorithm	Digital	Analogue
1n efficiency	30-47 %	20-25 %
2n efficiency	3-10 %	1-3 %

2 Neutron detection principles

2.1 Neutron detection

Unlike charged particles, which are slowed down mainly by the Coulomb interaction with the atoms of the material, and eventually ionizing them, neutrons have no charge, so they are not affected by the electromagnetic field, and do not produce direct ionization events. The only way they can interact with matter is through the nuclear force, characterized by a short range, being then effective only in the proximity of a nucleus (the nuclear radius is about 5 orders of magnitude smaller than the atomic one, giving a nuclear volume 10^{15} times smaller than the atomic one). Thus, a neutron in a material follows a straight path until, rarely, it "collides" with a nucleus and is, elastically, scattered in another direction. In each collision the neutron transfers some of his energy to the nucleus, finally being absorbed in the material whenever its velocity is sufficiently low. In a scintillator the scattered nuclei, due to electromagnetic interaction, excite the surrounding molecules that in turn reemit the absorbed energy through photons. These photons will be revealed in a photomultiplier (PM), that converts the light in current, via the photoelectric effect, and produces a signal.

2.2 Organic scintillators

As mentioned before, a scintillator is a material that exhibits the property of fluorescence when excited by an ionizing radiation, as a scattered nucleus or a γ ray. In the neutron elastic scattering, the maximum energy transfer to the nucleus occurs for an head-on collision, i.e. for $\theta = 0$, resulting in a maximum recoil energy of [7]

$$E_{R,max} = \frac{4A}{(1+A)^2} E_n \tag{2.1}$$

where A is the mass number of the target nucleus and E_n is the energy of the neutron (from 100 keV to 10 MeV for fast neutrons, produced in a fusion-evaporation reaction). Therefore, if the target nucleus is hydrogen, ^{1}H, the entire neutron energy can be transferred in a single scattering event, while a smaller maximum energy transfer results for heavier nuclei. For example, with ^{12}C ($A = 12$) $E_{R,max} \sim 28\%$ in a single scattering event.

As will be discussed in Section 2.3, the scintillating mechanism in organic materials arises also from transitions in the energy level structure of the molecules, making the fluorescence process observable in any of the aggregation states, compared to an inorganic scintillator which requires a crystalline structure for the scintillation process.

An organic scintillator has to fulfill one important requirement for scintillators: it is transparent to its own radiation. Under normal circumstances, at room temperature all the molecules of the scintillator are in the lowest vibrational state of the electronic ground state (S_{00} in Fig. 2.1). The thermal energy kT at room temperature is 0.025 eV, and thus according to the Boltzmann distribution $e^{-E/kT}$, it is unlikely to find any population of

the vibrational states above the electronic ground state. On the other hand, many possible vibrational states (S_{ij}) can be excited by the incoming radiation (and also many possible electronic excited states). These states decay fast ($\sim$ 1 ps) to the lowest vibrational state of the electronic excited state (S_{i0}), which then decays (in a time of the order of 10 ns) to one of the vibrational states of the electronic ground state (S_{0j}). Thus, from all the transitions, only the photon emitted from the decay to the lowest vibrational state of the electronic ground state (S_{00}) has any probability to be absorbed.

Solid organic scintillators usually have the highest light output (e.g. anthracene) and superior neutron-γ discrimination capabilities (e.g. stilbene). However, they are very expensive and difficult to assemble in samples larger than a few centimeters. Other disadvantages are deterioration of the crystals due to mechanical and thermal shock, and a difference as high as 25% in light output, depending on the orientation of the charged particles with respect to the crystal axis [7]. So, for the NEDA project, it has been decided to adopt an organic liquid scintillator.

NEDA will use the EJ301 scintillator. This scintillator has a maximum emission wavelength of 425 nm [8], and exhibits excellent pulse shape discrimination (PSD) properties, particularly for fast neutron counting and spectrometry in the presence of γ radiation. It is identical to the well known NE213 and BC501A, and therefore maintains all of the properties of those scintillators. EJ301 is composed of the PPO ($C_{15}H_{11}NO$) organic scintillator and to match the spectral sensitivity range of the PM uses as wavelength shifter POPOP ($C_{24}H_{16}N_2O$) dissolved in xylene (C_8H_{10}), an hydrocarbon consisting of a benzene ring with two methyl substituents. After being transferred to a cell or tank, it should be deoxygenated again by a bubbling process with pure nitrogen or argon immediately before sealing in order to achieve excellent PSD performance. The oxygen dissolved in the scintillator acts indeed as a non-radiating competitor with the electronic de-excitation pathway, absorbing the energy of the charged particle without emitting photons. This phenomenon, called *quenching*, reduces the light output and so the efficiency of the scintillator. Finally, the benzene needs to be treated very carefully, because of its toxicity and of its low Flash Point (T.O.C.) : 26 °C (79 °F).

2.3 Light Output

Organic scintillators produce light by the radiative decay of molecular states, which are excited by slowing down a charged particle. Referring to Figure 2.1, actually the excited state can be a singlet (spin=0) or, after the inter-system crossing, a triplet (spin=1) one. The transition from the singlet excited state to singlet ground state has, as said before, a life time typically of the order of nanoseconds, while the transition from the triplet excited state to the singlet ground state is of the order of milliseconds (due to the forbidden transitions from triplet states to singlet states). Molecules in triplet states can however interact pairwise resulting in one molecule in the ground state and one molecule in an excited singlet state, which then will decay. This interaction is much faster than the decay

of the triplet states, but still slower than the decay of the singlet states, and therefore the triplet states recombination will give rise to a slow component in the light collection from the scintillator material. If the particle that is stopped has a high specific energy loss, the density of the excited molecules will be very high, and there will be a greater interaction between the triplets, causing a larger slow component in the output from the scintillator. This is the principle behind neutron-γ discrimination.

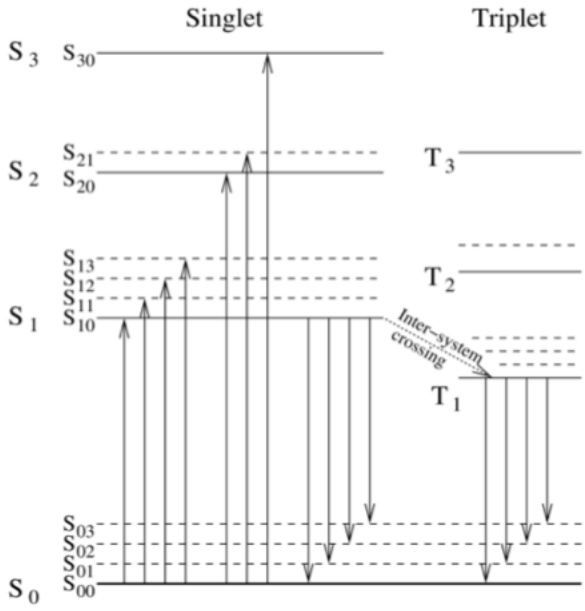

Figure 2.1: Energy states of molecules with π-electron structure. Figure taken from [7].

2.4 Signal production

After multiple reflections in the cylindrical inner wall of the detector cell (see Section 3.1), the light emitted by the scintillator is channeled through a crystal window into the PM tube. Here, through the photoelectric effect it turns into photoelectrons, which finally form the electrical signal that will be digitized with a fast sampling ADC (Analogue-Digital Converter) and then processed. The PMT typically consists of a photocathode of a bialkali metal alloy, a series of dynodes to multiply the photoelectrons and an anode to read out the signal (see Figure 2.2). Recently Hamamatsu has developed a new technology: using a fine tunned deposition process they could achieve ultra-pure photocathode materials and so ultra-pure bialkali photocathode PMTs, increasing the quantum efficiency (the percentage of photons hitting the device's photoreactive surface that produce charge carriers [7])

from ∼25% up to 43% [9]. This influences the photoelectron yield, which is of great importance for neutron-γ discrimination, as the quality of the discrimination is affected by the statistical fluctuation of the number of photoelectrons (Nphe) in the slow component of the scintillation pulse [10]. The Nphe clearly depends also on the number of photons per MeV and on the light collection from the scintillator. The Nphe per energy unit can be measured by comparing the position of the peak corresponding to a single photoelectron to the position of the Compton edge of γ ray emitted by a ^{137}Cs source [11].

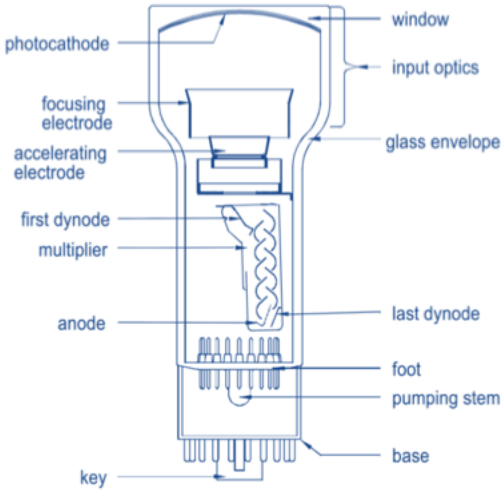

Figure 2.2: Scheme of a typical PMT design. Figure taken from [12].

2.5 Timing properties

The use of fast photomultipliers with good timing is necessary for two main reasons: first of all to disentangle the fast and slow decay components of the pulses in the pulse-shape analysis (PSA) in order to discriminate neutrons and γ rays (it will be discussed in Section 2.6); secondly to measure the time-of-flight between adjacent detectors in order to identify reaction channels with one or more neutrons emitted from scattered events.

In order to quantify the timing properties of the coupled setup (scintillator and PM), initially a constant fraction discriminator (CFD) algorithm was developed [13], since a simple leading edge discriminator would cause a dependence of the trigger time on the pulse amplitude (see Fig. 2.3), an effect called *time walk*. In fact, the CFD generates, for each signal, a trigger point independent of the peak height, when the leading edge of the pulse has reached a constant fraction of the pulse amplitude. The trigger time is taken at the zero-crossing point of a signal ZC_i , created by summing the original waveform S_i multiplied by a factor χ and its inverted signal delayed by an integer number of samples Δ:

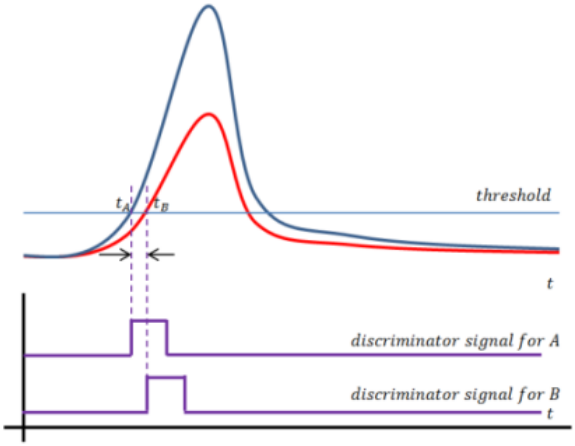

Figure 2.3: Schematic illustration of the time walk effect.

$$ZC_i = \chi(S_i - BS) - (S_{i-\Delta} - BS) \ . \tag{2.2}$$

The baseline BS is first calculated and then subtracted from both the delayed and scaled components. The zero-crossing point is then obtained by interpolating between the first negative sample and the preceding one, at a reference height of 5 mV over the baseline. The interpolation consists of a cubic spline employing 6 sampling points, with continuous first and second derivatives (C^2). The interpolating cubic function from k to $k+1$ was defined as:

$$P(x) = a_0(x-k)^3 + a_1(x-k)^2 + a_2(x-k) + a_3 \tag{2.3}$$

where

$$\begin{cases} a_0 = \frac{1}{30}(3y_{k-2} - 18y_{k-1} + 39y_k - 39y_{k+1} + 18y_{k+2} - 3y_{k+3}) \ , \\ a_1 = \frac{1}{30}(-7y_{k-2} + 42y_{k-1} - 71y_k + 46y_{k+1} - 12y_{k+2} + 2y_{k+3}) \ , \\ a_2 = \frac{1}{30}(4y_{k-2} - 24y_{k-1} + 2y_k + 23y_{k+1} - 6y_{k+2} + y_{k+3}) \ , \\ a_3 = y_k \ . \end{cases} \tag{2.4}$$

The particular coefficients are obtained calculating the derivative in k as $(y_{k+1} - y_{k-1})/2$. This improves significantly the time resolution with respect to the linear one and to the C^1 cubic spline, as the reported in [13]. The delay Δ and the factor χ are chosen in order to optimize the time resolution of the PM tube.

The trigger time for a signal from the prototype detector is then compared with the same one from a reference 1"×1" scintillator, BaF_2, presently the fastest known scintillator [14]. The rise time of the BaF_2 coupled with a R2059 PM is ∼1.3 ns, while the one of the R11833-100 used for the neutron detector is about 6.3 ns [13]. Thus, the uncertainty in the difference between the two trigger times mainly comes from the NEDA prototype.

The performance of the ZC algorithm 2.2 with a cubic interpolation 2.3, 2.4, is then compared to results obtained with a standard analog CFD.

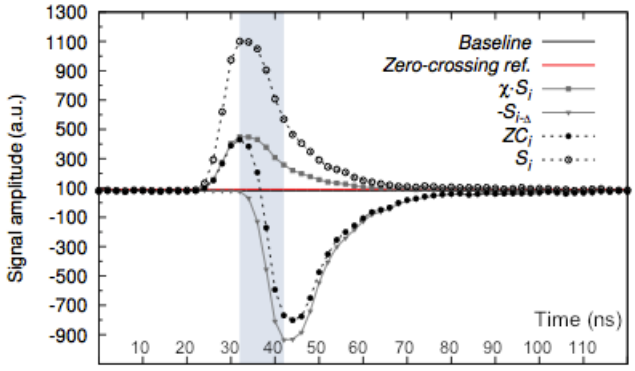

Figure 2.4: An example of a waveform and its zero-crossing signal. The horizontal black line is the baseline and the horizontal red line is the reference to get the zero-crossing. The grey area indicates the samples used for the cubic interpolation C^2. Figure taken from [13].

2.6 Pulse Shape Analysis

As explained in Section 2.3, since scattered nuclei have a higher specific energy loss than γ rays, the slow component of the former is greater, giving a difference in the pulse shape between an interacting γ ray and an interacting neutron (Fig. 2.5). This difference is used in both analogue and digital PSA to obtain a neutron-γ discrimination.

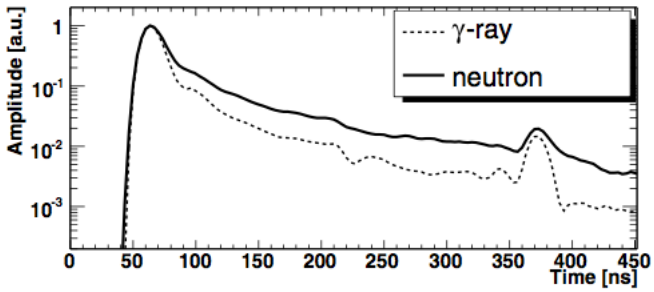

Figure 2.5: Pulse shapes from a BC501 liquid scintillator from a γ ray and a neutron interaction. Figure taken from [15].

Several sophisticated digital methods have been developed subsequently. Two conventional methods, similar to analog methods, are the *Charge Comparison* (CC) *method* and the *Integrated Rise-Time* (IRT) *method*, which will be discussed later. In order to

quantify the neutron-γ discrimination performances of the detector, a parameter named figure-of-merit (FOM) has been defined.

$$\mathrm{FOM} = \frac{S}{\mathrm{FWHM}_n + \mathrm{FWHM}_\gamma} \tag{2.5}$$

where S is the distance between the neutron and γ ray peaks in the distribution spectrum of the discrimination parameter, and FWHM_n and FWHM_γ are their full width at half maximum values. A larger value of FOM normally indicates a better performance of the neutron-γ discrimination. However, it should be noted that the FOM only measures the degree of separation that can be achieved between different types of event distributions and does not take into account any misidentification case [10]. For example, the misidentification due to *pile-up effect* (the overlapping of one signal with the following one) is quite common when the count rate is very high, but the two peaks are still well separated.

2.6.1 Charge Comparison method

The CC method identifies the particle by measuring the integrated charge over two different time regions of the signal pulse. The long integral (total charge) starts from the beginning of the pulse (8 ns before the CFD trigger point) to an optimized end point in the tail, while the short integral corresponding to the slow component is taken from an optimized start point after the pulse peak to the same end point as used for the long integral [10]. The optimal start point of the short integral, t_s, and the end point of both the short and long integrals, t_e, are determined carefully by performing a maximization of FOM value when leaving both t_s and t_e as free variables. The value of t_e has to be taken as short as possible for minimizing pile-up effects.

2.6.2 Integrated Rise-Time method

The IRT method can be considered as a digital implementation of the analog Zero-Crossover (ZCO) method since the integrated rise time can be evaluated directly by digital signal processing rather than first shaping it to extract the ZCO time. The rise time, defined as the time difference between the point when the integrated pulse crosses the 10% and the 90% of its maximal amplitude, is used as a parameter to distinguish neutrons from γ rays. The principle of this method is that the integrated rise time of the neutron-induced pulse is longer than that of the γ ray induced pulse.

In general, the IRT method performs slightly better than the CC method over most of the energy range (from 50 keVee to 1000 keVee, keV electron equivalent, corresponds to the light emitted when an electron loses 1 keV), with a FOM value on average about 7% higher [10]. This is probably because the IRT method can cancel out part of the high-frequency noise present in the signal by integrating the pulse. However, in [10] it is noted that at low energy, under 100 keVee, there is a deterioration in the neutron-γ

discrimination performance, resulting from the fact that the signal-to-noise ratio is quite low due to the scintillation statistics, the electronic noise and the quantization effect of the digitizer, which is a fundamental limitation for any discrimination method [16].

3 The NEDA detector: first tests

3.1 Description of the detector and the setup

Each detector that will form NEDA is contained in an hexagonal shaped aluminium housing with a thickness of 2 mm, a length of 200 mm and an edge length of 80.8 mm (see Fig. 3.1), containing about 3 liters of EJ301 liquid scintillator. It will be placed at about 1 m from the target, giving an angular coverage of about 7°. It is foreseen that, due to the larger distance, the loss from neighbor rejection decreases to 2% and 3.5% for 2n and 3n channels respectively (channels with emission of 2 or 3 neutrons) [17]. The optimization of the length has also been studied in [18], and the result is that the detection efficiency ϵ_n, that is the ratio of neutrons detected to neutrons emitted, reaches a constant value of 80-95% for a length between 20 and 40 cm, depending on the neutron energy and the scintillator type. Studying the depth distributions, the significant interactions mainly occur in the first layers of the scintillator. In order to minimize the probability of cross-talk, the optimal length for the detector is 20 cm, with a detection probability of the order of 70% and a diameter corresponding to the largest PM tubes easily available, which is 5 inches. The inner

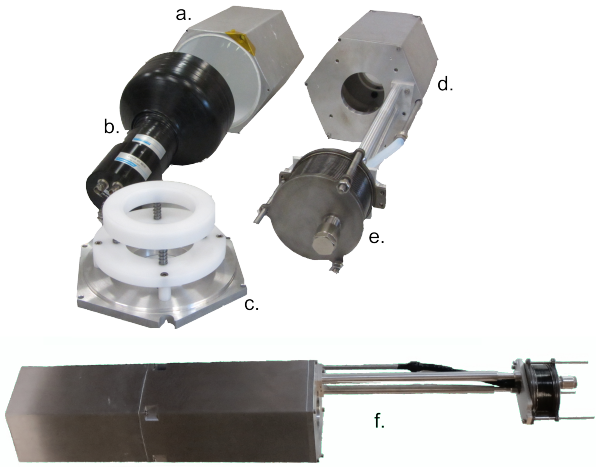

Figure 3.1: NEDA detector prototype. Above are shown the single parts which constitute the detector: (a) hexagonal cell containing the EJ301 scintillator; (b) R11833-100 PM; (c) holding cover for the PM; (d) hexagonal case for the PM; (e) expansion bellows for the liquid scintillator. μ-metal is within the hexagonal case of the PM. Below (f) it is shown the mounted prototype.

wall of the cylindrical detector has been sandblasted and painted with a xylene resistant paint, so that the light hitting the surface would reflect, increasing the light collection. The latter is glued to the aluminium housing with a particular sealing and then a R11833-100 superbialkali PMT from Hamamatsu is mounted on the top using an optical grease with

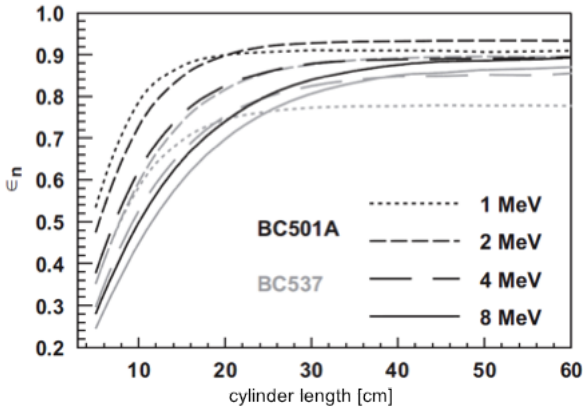

Figure 3.2: Detection efficiency as a function of the cylindrical detector depth. The black and grey colors differentiate the trend of the different scintillators (EJ301 is identical to BC501A). Figure taken from [18].

the same diffusion coefficient of the crystal window of the detector and of the PM. The photomultiplier is surrounded by a foil of μ-metal, in order to shield from the external electromagnetic field, including the Earth one, which influences its operation. A bellows, connected to the cylindrical detector through a stainless steel tube, keeps the scintillator at a constants pressure, expanding or contracting in according to the temperature. To digitize the signals from the detectors two STRUCK digitizers are employed. One digitizer, used for digitizing the waveforms from the detectors, is a SIS3350 unit which has four channels with a sampling frequency of 500 MS/s (MegaSamples/s) and a bit resolution of 20 bits. This sampling frequency and bit resolution has been shown to be sufficient for pulse-shape analysis of the signals from liquid scintillator detector [19]. The other digitizer, used to digitized the signals from the time-to-amplitude converters and the analogue pulse-shape discrimination unit, is a SIS3302 unit which has 8 channels with a sampling frequency of 100 MS/s and a bit resolution of 16 bits. The analogue pulse-shape discrimination is carried out using a BARTEK NDE202 unit, the same unit that is currently used in the Neutron Wall detector array. The digitizers communicate with the data acquisition system via a VME controller using an optical link.

3.2 Timing tests

In this first part, the timing properties of the new detector will be discussed. All the measurements were carried out at INFN-LNL. The experimental setup is illustrated in Fig. 3.3. A ^{60}Co source was placed at 25 cm from the front face of the NEDA detector and at 3 cm from the cylindrical 1"$\times$1" BaF_2. The two γ rays from ^{60}Co are emitted with a difference in time less than 1 ps, which is absolutely negligible for the time accuracy of

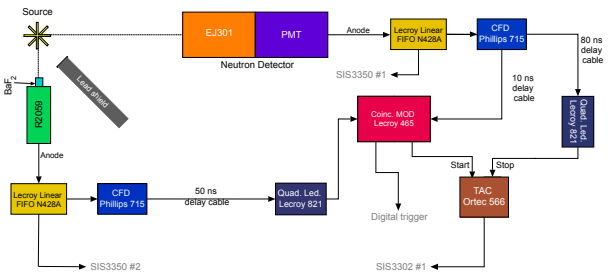

Figure 3.3: Schematic picture of the setup employed for the pulse-timing measurements.

the system. They are then considered simultaneous, and a coincidence measurement can be performed between the two detectors, using the BaF_2 as a reference. The detectors were placed at an angle of about 90° with respect to the outgoing γ rays. A 5 cm thick lead brick was placed between the neutron detector and BaF_2, in order to minimize the detection of γ rays that were scattered from one detector into the other. A particular attention was payed to ensure that the lead shield did not shadow the detectors from the ^{60}Co source. The high voltage (HV) for the Hamamatsu PMT was set to get an anode signal amplitude of about 1 V/MeV, while the HV for the BaF_2 PMT was set to 2.0 kV. The anode signals from the detectors were connected to LeCroy N428A linear fan-in/fan-out units, from which the output signals were sent to the sampling ADCs and to analog CFD units of type Phillips 715. The thresholds and shaping delays of the CFD for the two PMTs were -102 mV and 5 ns for the BaF_2, -40 mV and 11 ns for the neutron detector. The thresholds were adjusted to the minimum and the shaping delays were optimized to obtain the best possible time resolutions. The data collection was done with a count rate of $\sim$ 3.5 kHz, and a coincidence rate of about 27 Hz. The analog time difference between the EJ301 and BaF_2 detectors was obtained by using an Ortec 566 TAC (500 ns range). The start and stop signals of the TAC were the CFD signals from the coincidence unit and from the neutron detector, respectively. For the stop signal a delay of 80 ns was used. The start signal was only produced if it overlapped in time with a wide neutron detector signal in the coincidence unit LeCroy 465. A signal from this unit was also used as a trigger for the digital data acquisition system. The detector waveforms were digitized by the sampling ADC Struck SIS3350, a VME unit with four channels, each with a sampling rate of 500 MS/s, a resolution of 12 bit and a dynamic range of 2 V. The analog output signal from the TAC was digitized by a Struck SIS3302 sampling ADC. The digitizers were readout through the VME bus and the data were sent to the data acquisition system via a Struck SIS3350 controller using an optical link. The pulse-timing properties were studied at the sampling rate of 500 MS/s.

3.2.1 Digital timing

The ZC algorithm already described in Section 2.5 was used. First of all the two parameters χ and Δ were optimized. The baseline BS was obtained from the average of the counts of channels between 5 and 50. We have considered 10 000 events and for these the time difference between the EJ301 and the BaF_2 detectors was calculated and we have checked the quality of its gaussian interpolation. The difference in channels was easily translated in difference in time, since a sampling rate of 500 MS/s is equivalent to one sample (channel) every 2 ns. The results of the parameters optimization were 3 ns for Δ and 0.37 for χ. Then, 100 000 events with this parameters were considered and the difference between the neutron detector and BaF_2 Zero Crossing was interpolated combining a gaussian function and two exponential functions for the tails (see Fig. 3.4). The gaussian function was defined as

$$y = \frac{a_0}{\sqrt{2\pi}\sigma} e^{-\frac{(x-b_0)^2}{2\sigma^2}} \ , \tag{3.1}$$

while the exponential functions as

$$exp_1(x) = \frac{a_0}{\sqrt{2\pi}\sigma} e^{\frac{(b_1-b_0)^2}{2\sigma^2}} e^{-\frac{(b_1-b_0)(x-b_0)}{\sigma^2}} \ , \tag{3.2}$$

$$exp_2(x) = \frac{a_0}{\sqrt{2\pi}\sigma} e^{\frac{(b_2-b_0)^2}{2\sigma^2}} e^{-\frac{(b_2-b_0)(x-b_0)}{\sigma^2}} \ . \tag{3.3}$$

Two parameters, b_1 and b_2, were defined and then optimized during the fit, delimiting the region for the gaussian fit and the exponential tails. The centroid b_0 is not of interest, and it depends basically on the distance from the γ source and electronic delay. The FWHM was extracted as the difference between $hwhm_2(b_2)$ and $hwhm_1(b_1)$, where

$$hwhm_2(b_2) = \begin{cases} \frac{1}{2}(b_0+b_2) + \frac{\ln(2)\sigma^2}{(b_2-b_0)} & \text{if } b_2 < b_0 + \sigma\sqrt{2\ln(2)} \ , \\ b_0 + \sigma\sqrt{2\ln(2)} & \text{if } b_2 > b_0 + \sigma\sqrt{2\ln(2)} \ , \end{cases} \tag{3.4}$$

and

$$hwhm_1(b_1) = \begin{cases} \frac{1}{2}(b_1+b_0) + \frac{\ln(2)\sigma^2}{(b_1-b_0)} & \text{if } b_1 > b_0 - \sigma\sqrt{2\ln(2)} \ , \\ b_0 - \sigma\sqrt{2\ln(2)} & \text{if } b_1 < b_0 - \sigma\sqrt{2\ln(2)} \ . \end{cases} \tag{3.5}$$

The final result was, as shown in Fig. 3.4, a FWHM = 1113 ± 14 ps.

The timing properties versus the signal amplitude was also studied. We had to proceed then to an energy calibration. Four γ ray sources, ^{22}Na, ^{60}Co, ^{137}Cs and ^{241}Am, were used (see Table 3.1). As a reference point to calibrate the ADC channels we used the Compton edge, defined as the channel corresponding to around 90% of the peak height in the Compton distribution according to the simulations performed in Ref. [18]. After a linear interpolation (see Fig. 3.5) the energy to channel ratio was obtained, equal to 1.102 ± 0.004 keV/ch. For all sources besides the ^{60}Co, the Compton edge channel was calculated

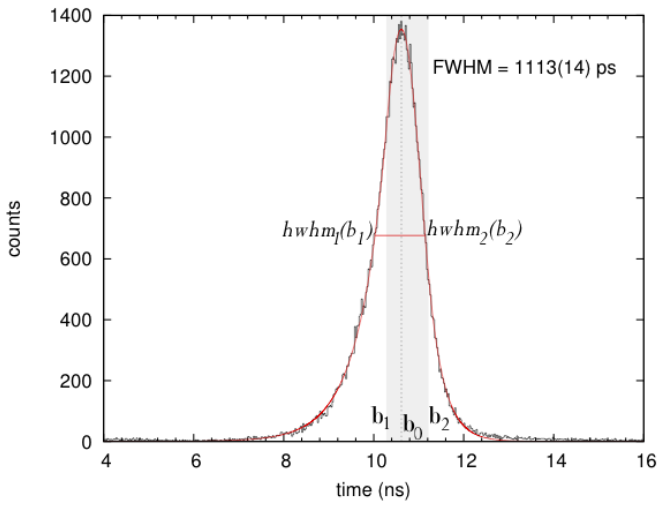

Figure 3.4: Plot of the time difference between the NEDA prototype and the BaF_2 detectors for 100 000 events. The grey area delimits the central region, where a gaussian fit was performed, from the two exponential tails. The number in bracket is the error of the time resolution for the calculated FWHM.

Table 3.1: The γ rays emitted by the sources used for calibration of the EJ301 detector.

Source	**γ ray energy (keV)**	**Compton edge (keV)**
^{22}Na	511, 1275	341, 1062
^{60}Co	1173, 1332	1041 (average)
^{137}Cs	662	478
^{241}Am	59.5	-

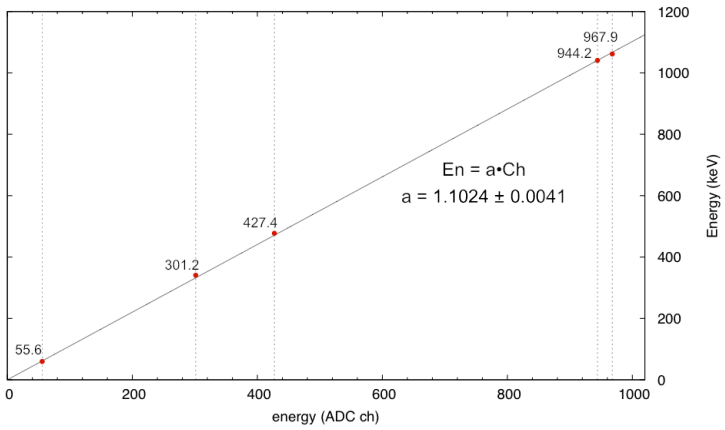

Figure 3.5: Energy calibration from γ sources listed in Table 3.1.

after background subtraction. The background was normalized using the acquisition time:

$$norm = \frac{\mathrm{T}_{source}}{\mathrm{T}_{bkg}} \frac{\mathrm{N}_{bkg}}{\mathrm{N}_{source}} \ , \tag{3.6}$$

where $norm$ is the normalization constant, T_{source}, T_{bkg}, N_{source} and N_{bkg} are the acquisition time and the total number of events for the source or for the background, respectively. This normalization could not be performed with ^{60}Co, since for this source the data was collected using the coincidence between neutron detector and BaF_2 as trigger, while for the other sources and the background the trigger came only from the neutron detector. Having different trigger conditions the data collection from ^{60}Co could not be comparated with the data collection of the background. However the result of the fit was good. In Fig. 3.6, as an example, the energy spectrum for the ^{22}Na source is shown.

Once the energy calibration was performed, it was possible to study the time resolution as a function of the energy. Different cuts in energy were performed starting from 50 keVee up to 1400 keVee, with a width of 150 keVee. For each energy range the FWHM was calculated in the same way as for the 100 000 events (Fig. 3.4). The results are displayed in Fig. 3.7. Using a constant fraction timing the dependence of the time resolution from the energy should follow an $1/\sqrt{E}$ behavior [20], and this is reflected in our reults. For energies higher than 1000 keVee there is a deterioration of the time resolution: for such events there is an higher probability that a high energy event scatters twice or more in the detector, resulting in a worse time resolution. The light is produced in two (or more) different locations inside the scintillator. Figure 3.8 shows an example for an energy cut centered at 1025 keVee, that gives FWHM $= 915 \pm 21$ ps.

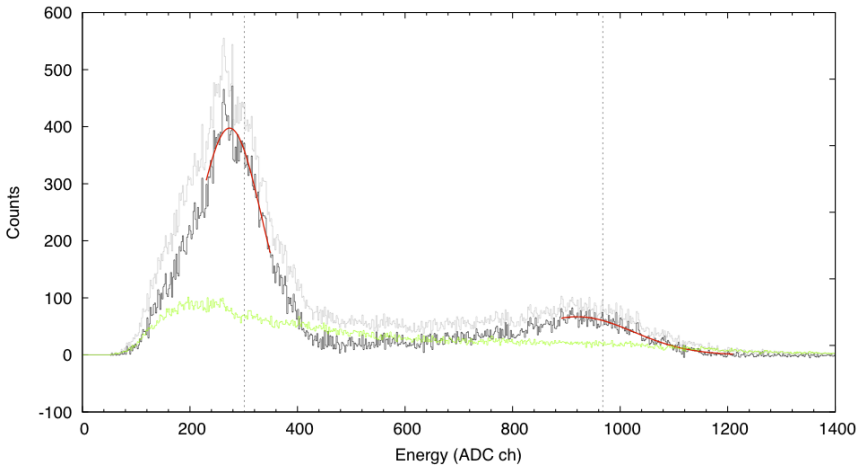

Figure 3.6: Energy spectrum of ^{22}Na and gaussian fit of its two Compton edges. The grey line is the original spectrum, the green one is the background normalized using the acquisition time, and the black line is the source spectrum after background subtraction. In red are highlighted the gaussian fits of the peaks, and the dashed lines show the position of the true Compton edge.

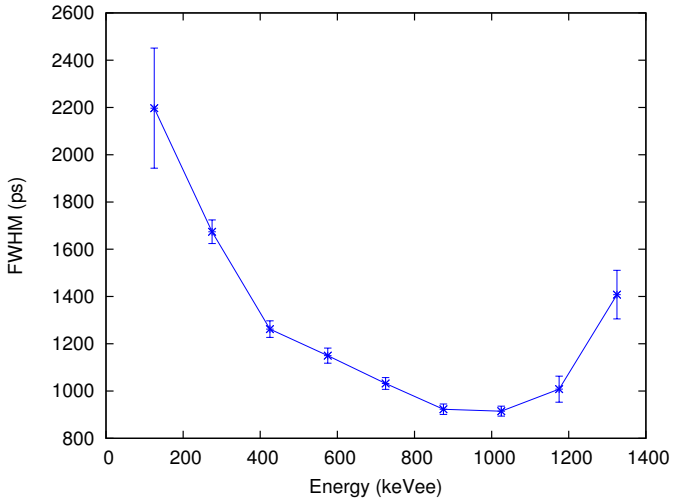

Figure 3.7: Time resolution versus energy. Cuts are made every 150 keVee, from 50 keVee to 1400 keVee.

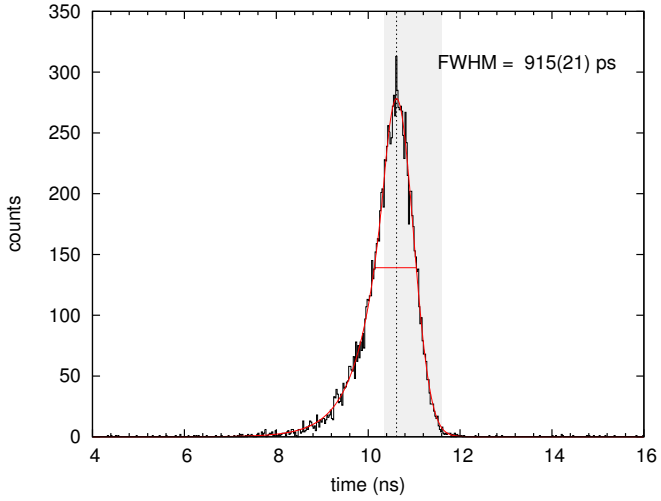

Figure 3.8: Time resolution for the signals with energies between 950 and 1100 keVee.

3.2.2 Analog timing

In this section the analog timing analysis is performed and then compared to the digital one. Using the standard analog CFD module, a time calibration is needed to derive the correlation between channels and time. The signal from one detector has been measured, using the same detector both as start and as stop, changing progressively the length of a calibrated delay cable for the stop. (see Fig. 3.9). The measured difference in time for each delay was exclusively depending on the length of the cable used for the stop, since the signal from the detector was exactly the same. With a linear interpolation the time

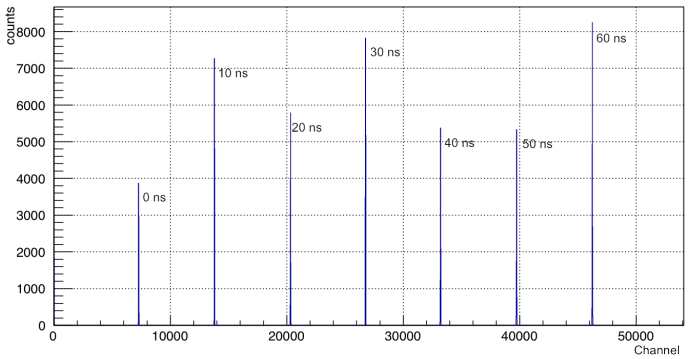

Figure 3.9: Time calibration spectrum. The signals are separated by 10 ns.

to channel calibration was obtained, as shown in Fig. 3.10. Since we are interested in the

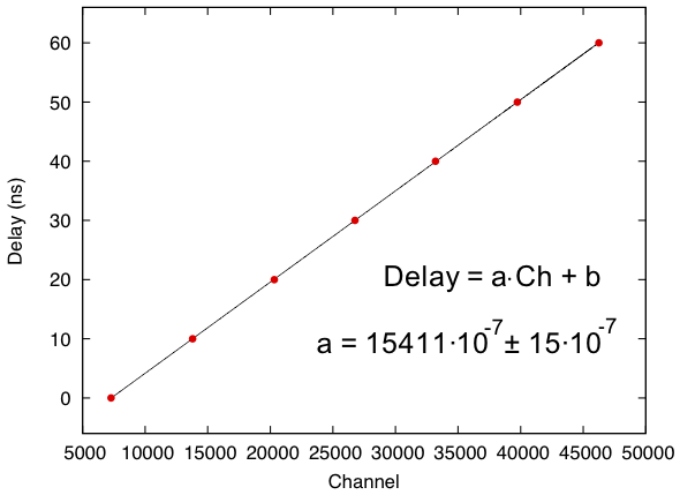

Figure 3.10: Time calibration of the setup.

time difference between the neutron detector and the BaF_2 detectors, in the interpolation procedure $Time(ns) = a \cdot Ch + b$ only the coefficient a between channels and time delay is relevant, which results in $a = 15.41 \cdot 10^{-4} \pm 0.02 \cdot 10^{-4}$ ns/ch. The remaining term b depends only on the internal delay of the setup.

As for the digital timing in Section 3.2.1, the total analog time resolution for 100 000 events was estimated and the result is shown in Fig. 3.11. Compared to the digital time resolution, 1113 ± 14 ps, the analog one is slightly better, 1036 ± 35 ps.

Also in this case different energy cuts were performed, to study the dependence of the time resolution from the energy deposited in the detector. The energy windows were exactly the same as before, from 50 keVee up to 1400 keVee, with a width of 150 keVee. The best resolution is still obtained for energies between 950 and 1100 keVee, with a FWHM $= 817 \pm 20$ ps, Fig. 3.12, to be compared to a FWHM $= 915 \pm 21$ ps obtained with digital timing. The same trend obtained in the digital analysis is observed, as it is clear from Fig. 3.13 where the two are compared. The analog analysis results always slightly better (≈100 ps) for almost all energies. In a previous study [13] the digital analysis for high energies (above 600 keVee) resulted in a slightly better resolution with respect to the analog one, and overall better performances were obtained (Fig. 3.14). However, the detector was 5"×5" (12.7 cm × 12.7 cm), significantly smaller than the NEDA detector prototype (20 cm × 12.7 cm). This consistently affects the light collection and consequently the time resolution of the detector. The general trend is anyway respected. In Table 3.2 a comparison between the NEDA detector prototype and a 5"×5" detector [13] coupled with the same PM, R11833-100, is reported. The FWHM is the one calculated over the total

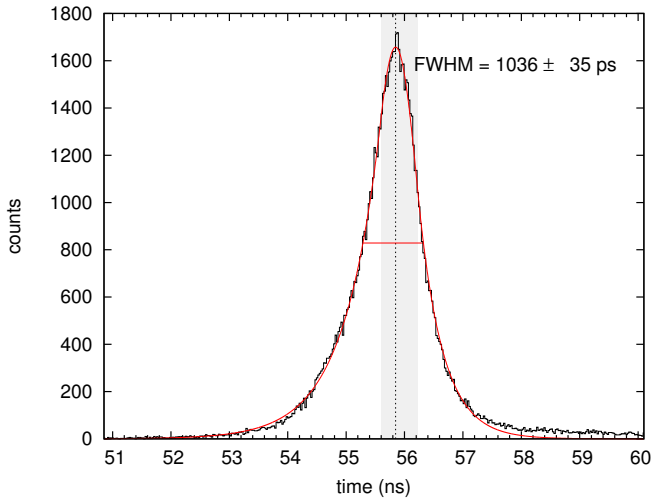

Figure 3.11: Plot of the analog time difference between the NEDA prototype and the BaF_2 detector for 100 000 events.

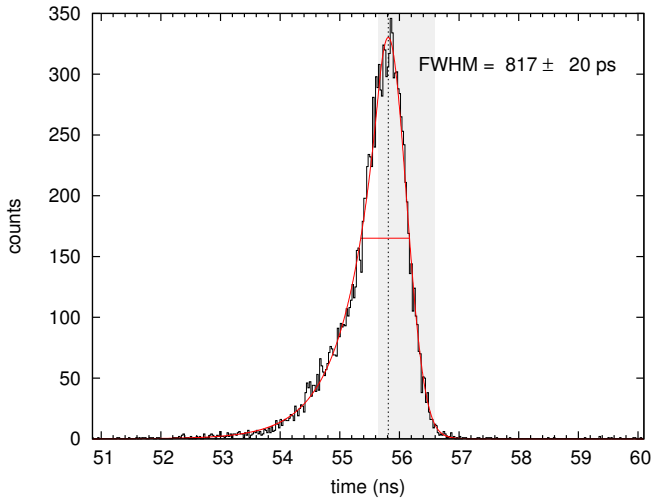

Figure 3.12: Plot of the analog time difference between the NEDA prototype and the BaF_2 detectors for energies between 950 and 1100 keVee.

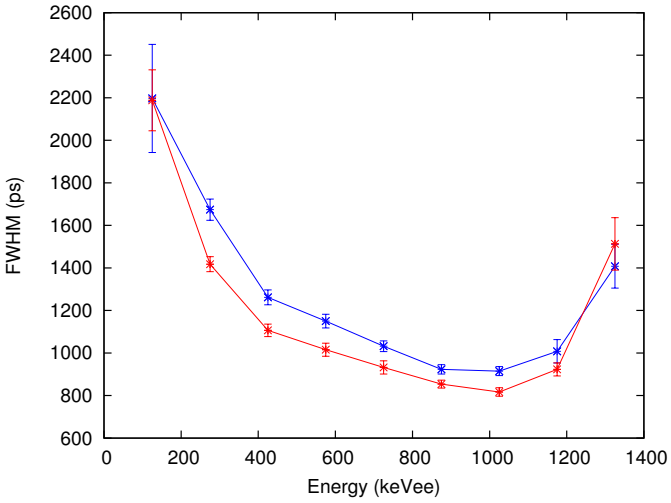

Figure 3.13: Time resolution versus energy for the digital (blue) and analog (red) analysis of the NEDA detector prototype.

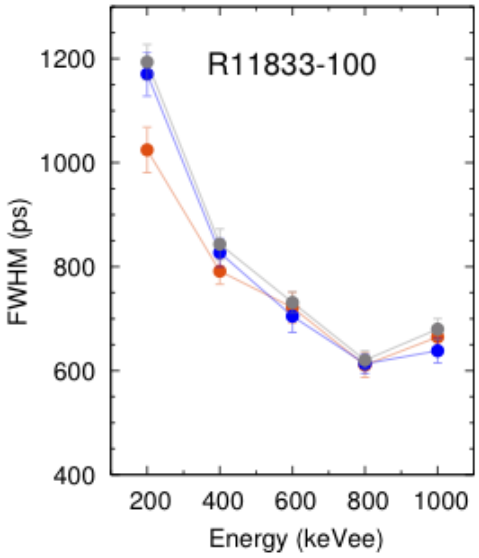

Figure 3.14: Time resolution as a function of energy for a 500 MS/s digital (blue) and analog (red) analysis of the same 5"×5" neutron detector from [13]. In grey are also reported the data for 200 MS/s digital analysis simulation. The digital analysis was performed using the same algorithm as the one of this work.

energy range.

Table 3.2: Comparison between the NEDA detector prototype and the 5"×5" BC501A liquid scintillator detector from [13].

Detector	$\mathbf{N}_{phe}$ **(MeV^{-1})**	**Digital FWHM (ps)**	**Analog FWHM (ps)**
5"×5" BC501A	1830(90)	730(20)	743(13)
NEDA prototype	$\sim$ 2200	1113(14)	1036(35)

3.3 Pulse Shape Analysis tests

In this section the results of a preliminary test of a Pulse Shape Analysis with the Charge Comparison method will be presented. A ^{252}Cf source was placed at 1 m from the neutron detector prototype (to simulate the final staircase configuration of the array) and at 10 cm from the BaF_2 detector. The setup was the same as for the timing analysis (see Fig. 3.3), except for the stop signal of the BaF_2 detector that was delayed of 152 ns. A BARTEK Z/C TAC module was also added after the CFD of the neutron detector, which gives the analog Z/C (zero cross over). The coincidence condition was an event detected in the NEDA detector and in the BaF_2 within a time window of 162 ns. The trigger frequency was $\sim$ 10 Hz, with a neutron detection of almost 1 neutron every 2 seconds. To have $\sim$ 1 V for 1 MeVee the high voltage was set at -1288 V, while for the BaF_2 it was set at 2.0 kV as in the timing measurements. The threshold and shaping delays of the CFD for the two PMTs were -135 mV and 5 ns for the BaF_2, -35 mV and 11 ns for the neutron detector.

As explained in Section 2.6.1, the CC method consists in calculating the charge distributed in the slow component of the pulse and comparing it with the total charge of the signal. Since neutrons produces more delayed photoelectrons than γ rays (see Section 2.3), their slow component value should be higher than the one from γ rays. Actually, the slow component was compared to the charge between 2 channels below the threshold and 10 channels above the threshold (fast component). For the slow component 250 channels were taken after the fast component, and the baseline was extracted by averaging the first 300 channels. Figure 3.15 shows the slow component versus the fast component. It is clear that at higher energies (higher charge) there is a more defined separation of the events into two different blobs, with different slow to fast component ratio. The higher blob has an higher ratio: the slow component is higher than in the other blob, and therefore these events correspond to a neutron interacting with the scintillator, while the second blob contains γ events. The more the two blobs are separated, the better neutron-γ discrimination efficiency the detector has. If we plot the ratio between the two components, two peaks are obtained (see Fig. 3.16). After fitting each peak and extracting the centroid position

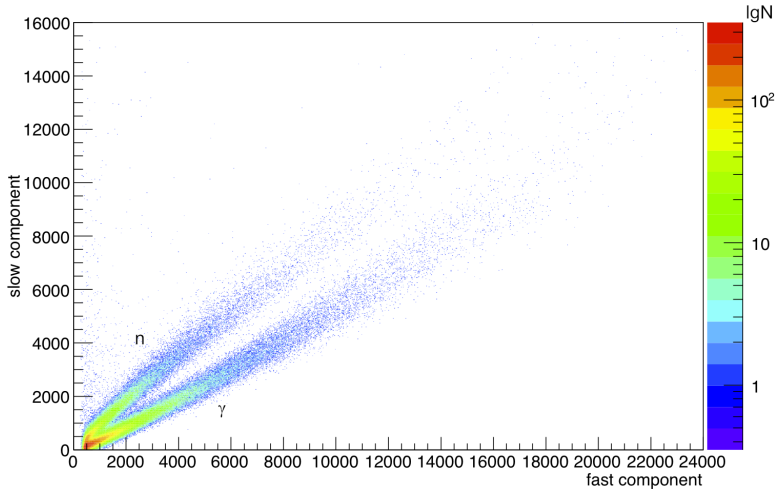

Figure 3.15: Density plot of the slow component versus the fast component for each pulse. No energy threshold was set in the analysis.

and FWHM, the FOM value can be obtained, as mentioned in equation 2.5. In particular, the fit was done defining two gaussian functions and two exponential tails:

$$\begin{cases} g_1(x) = \frac{a_{0,1}}{\sqrt{2\pi}\sigma_1} e^{-\frac{(x-b_{0,1})^2}{2{\sigma_1}^2}}, \\ g_2(x) = \frac{a_{0,2}}{\sqrt{2\pi}\sigma_2} e^{-\frac{(x-b_{0,2})^2}{2{\sigma_2}^2}}, \\ exp_1(x) = \frac{a_{0,1}}{\sqrt{2\pi}\sigma_1} e^{\frac{(b_1-b_{0,1})^2}{2{\sigma_1}^2}} e^{-\frac{(b_1-b_{0,1})(x-b_{0,1})}{{\sigma_1}^2}}, \\ exp_2(x) = \frac{a_{0,2}}{\sqrt{2\pi}\sigma_2} e^{\frac{(b_2-b_{0,2})^2}{2{\sigma_2}^2}} e^{-\frac{(b_2-b_{0,2})(x-b_{0,2})}{{\sigma_2}^2}}. \end{cases} \tag{3.7}$$

Two parameter b_1 and b_2 were optimized to define the region where the sum of the two gaussian functions are used, while below b_1 and above b_2 exp_1 and exp_2 were used, respectively. The FOM results in 0.84 ± 0.01.

Neutrons and γ rays can often be distinguished with high accuracy by measuring their TOF between the emission point and the detector. The TOF parameter was used here combined with the CC method to qualitatively evaluate its discrimination quality. Density plot of the neutron-γ discrimination parameter of the CC method versus the TOF measurement is shown in Fig. 3.17. Two distinct clusters of events are clearly visible centered at TOF values of $\sim$ -17 and $\sim$ 26 ns, corresponding to γ rays and neutrons, respectively. The neutron-γ discrimination results of the CC method is therefore similar to that of TOF measurement, demonstrating qualitatively the correctness of this method. However, there are some other events located elsewhere, most of which are random and pile-up events. It

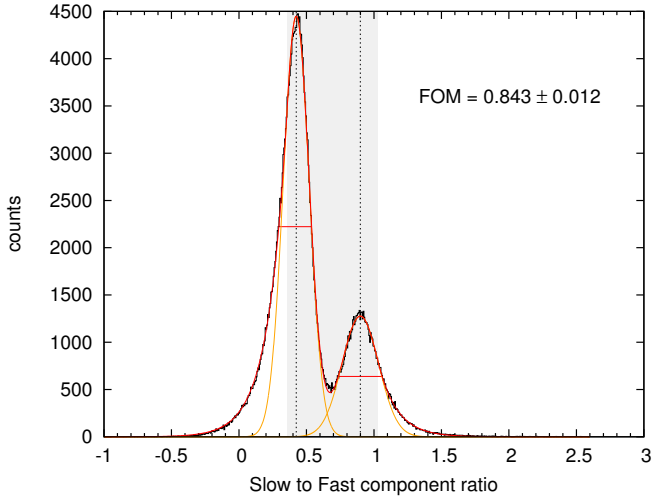

Figure 3.16: Neutron-γ discrimination spectrum using the CC method. Also the interpolating function (red) and the two single gaussian distributions (orange) are shown. The two red lines indicate the FWHM for each peak, while the grey area shows the region between b_1 and b_2.

is always suggested that pulse-shape discrimination and TOF measurement should complement each other for a better neutron-γ discrimination.

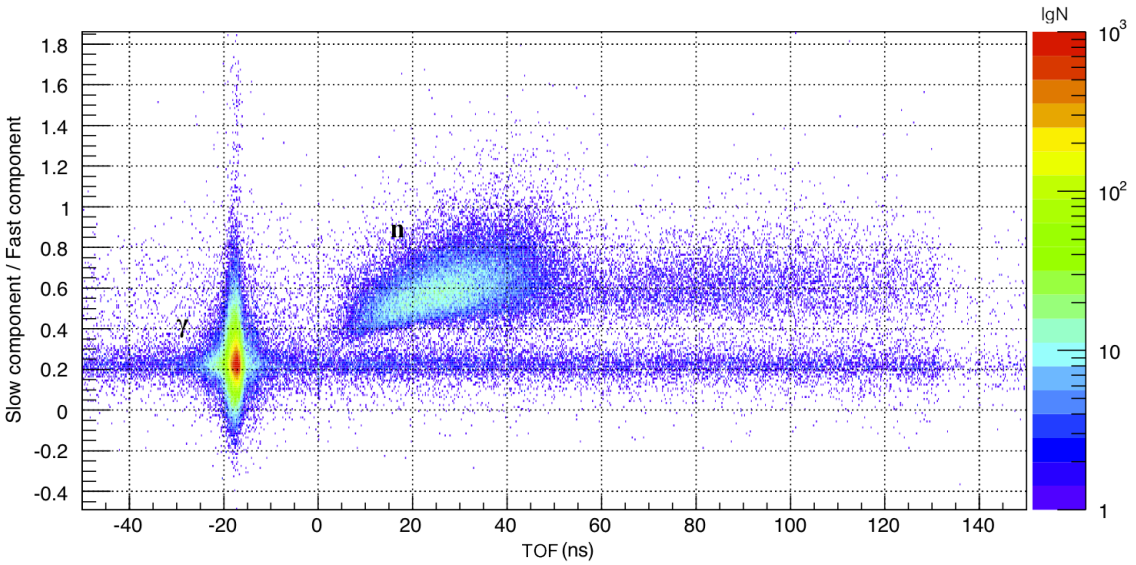

Figure 3.17: Density plot of the discrimination parameter of the CC method versus the TOF for each event. No energy threshold was set in the analysis.

4 Summary and Conclusions

The first study of the performances of the NEDA detector prototype, both in timing and in neutron-γ discrimination, was performed. The NEDA detector was coupled to a 5 inches super bialkali Hamamatsu R11833-100 photomultiplier tube, which is the final PM chosen for NEDA. The liquid scintillator EJ301 is used, which has the best characteristics for neutron detection. However, due to its toxicity and its chemical reactivity it has to be threated very carefully, paying also attention that it is not contaminated by other materials. One should also avoid the contact with air, since the oxygen solved in it significantly decreases the light output (quenching). However, in the filling and bubbling procedures a lot of attention was payed, and the final number of photoelectron produced was quite high (~ 2200 MeV^{-1}). This increases the signal resolution, both digitally and analogically. The analysis of the waveforms were performed digitally with a SIS3350 digitizer with a sampling rate of 500 MS/s and 12-bit resolution, and also analogically using a CFD unit of type Philipps 715, a coincidence module Lecroy 465 and a TAC Ortec 566. The analog output signal from the TAC was digitized by a SIS3302 sampling ADC with a sampling rate of 100 MS/s and 16-bit resolution. A BARTEK Z/C TAC module was also used in pulse-shape analysis.

For the digital analysis, a constant fraction discriminator algorithm has been used, consisting of a zero-crossing signal obtained as a cubic spline interpolation continuous to the second derivative. The obtained time resolution was compared to that obtained with a standard analog CFD. Different cuts in energy were performed, to study the time resolution as a function of energy. The general trend following $1/\sqrt{E}$ is respected, with the digital timing resulting almost always in a worse resolution than in the analog case, by about 100 ps (915 ± 21 versus 817 ± 20 for energies between 950 and 1100 keVee). Compared to the time resolution of a 5"$\times$5" detector filled with the same liquid scintillator and the same PM, the average digital FWHM of the prototype is of ~ 400 ps higher, while the analog one of ~ 300 ps. However, in the energy range with the best performances the difference in time resolution is of 300 ps (digital) and 200 ps (analog). Taking into account that for a larger detector a worse resolution is indeed expected, the results for the NEDA prototype are acceptable.

In the analysis of the pulse-shape, a ^{252}Cf source was used. This was placed at 1 m from the detector, in order to simulate the final setup of the full array. A Charge Comparison method was preliminary implemented, calculating the sum from the 10th to the 260th sample after the threshold (slow component) and the sum from 2 channels below to 10 channels above the threshold (fast component). Preliminary, the average baseline was calculated and subtracted, by averaging the first 300 channels. The neutron-γ discrimination parameter resulted to be in FOM $= 0.84 \pm 0.01$, but a comparison with other results can not be done yet, since the method has still to be optimized in many aspects, as for example the choice of the range for the fast component and the slow component. When plotting the slow to fast component ratio, one can notice that there are some negative

values. Another evidence that the algorithm implemented so far is not working properly is the fact that the total charge integral at a certain point was decreasing. All these aspects has of course to be investigated. A way to improve the analysis can be the use of a cubic interpolation to calculate the integrals. Thus, the starting and the ending point of each sum would be exactly the same for each event, not depending on the discretization from the ADC, and the final computation should be more precise. Energy cuts also have to be performed to obtain the FOM as a function of the energy.

In any case, though further studies are going on, this preliminary test of the first NEDA prototype are very promising for this new generation neutron detector array.

References

[1] Ö. Skeppstedt et al. *The EUROBALL neutron wall - design and performance tests of neutron detectors*. Nucl. Instrum. Meth., 1999.

[2] J. Simpson et al. Acta Phys Hung. N. S., 2000.

[3] D. Mengoni et al. Annual Report LNL, 2014.

[4] S. Akkoyun et al. *AGATA ‚Äî advanced gamma tracking array*. Nucl. Instrum. Meth., 2012, pp. 26–58.

[5] T. Hüyük. Nucl. Instrum. Meth., to be submitted.

[6] J.J. Valiente-Dobón. *NEDA: Neutron Detector Array*. report.

[7] G.F. Knoll. *Radiation Detection and Measurement- 3rd edition*. John Wiley and Sons, 1999.

[8] ELJEN Technology. *EJ-301*. URL: `http://www.eljentechnology.com/index.php/products/liquid-scintillators/71-ej-301`.

[9] D. Renker. *New developments on photosensors for particle physics*. Nucl. Instrum. Meth., 2009.

[10] X. L. Luo, V. Modamio, J. Nyberg, et al. *Test of digital neutron-gamma discrimination with four different photomultiplier tubes for the NEutron Detector Array (NEDA)*. 2014.

[11] M. Moszyński, G. Costa, G. Guillaume, et al. Nucl. Instrum. Meth., 1991.

[12] M.L. El-Sheikh. *Design and Simulation of Neutron Detectors*. M. S. thesis, KTH, 2009.

[13] V. Modamio, J.J. Valiente-Dobón, G. Jaworski, et al. *Digital pulse-timing techniques for the neutron detector array NEDA*. Nucl. Instrum. Meth., June 5, 2014.

[14] Saint-Gobain Ceramics & Plastics. *BaF_2, Barium Fluoride*. Apr. 2014. URL: `http://www.crystals.saint-gobain.com/uploadedFiles/SG-Crystals/Documents/Barium%20Fluoride%20Data%20Sheet.pdf`.

[15] Pär-Anders Söderström. *Collective Structure of Neutron-Rich Rare-Earth Nuclei and Development of Instrumentation for Gamma-Ray Spectroscopy*. Digital Comprehensive Summaries of Uppsala Dissertations from the Faculty of Science and Technology 818, 2011.

[16] X.L. Luo, Y.K. Wang, G. Lui, et al. Nucl. Instrum. Meth., 2013.

[17] B. De Canditiis. *Studio della configurazione 2π dell'array NEDA attraverso simulazioni di Monte Carlo di reazione di fusione-evaporazione*. Tesi di Laurea Triennale, 2012.

[18] G. Jaworski et al. Nucl. Instrum. Meth. A 673, 2012, p. 64.

[19] Pär-Anders Söderström et al. *Digital pulse-shape discrimination of fast neutrons and γ rays*. Nucl. Instrum. Meth., 2008.

[20] B. Bengtson and M. Moszyński. *Timing properties of scintillation counters*. Nucl. Instrum. Meth. 81, 1970, pp. 109–120.